

ARTICLE OPEN



Mechanism of keyhole pore formation in metal additive manufacturing

Lu Wang ¹, Yanming Zhang ¹, Hou Yi Chia ¹ and Wentao Yan ¹✉

During metal additive manufacturing, the porosity of the as-built part deteriorates the mechanical property and even hinders the further application of metal additive manufacturing. Particularly, the mechanisms of keyhole pores associated with the keyhole fluctuation are not fully understood. To reveal the mechanisms of the keyhole pores formation, we adopt a multiphysics thermal-fluid flow model incorporating heat transfer, liquid flow, metal evaporation, Marangoni effect, and Darcy's law to simulate the keyhole pore formation process, and the results are validated with the in situ X-ray images. The simulation results present the instant bubble formation due to the keyhole instability and motion of the instant bubble pinning on the solidification front. Furthermore, comparing the keyhole pore formation under different laser scanning speeds shows that the keyhole pore is sensitive to the manufacturing parameters. Additionally, the simulation under a low ambient pressure shows the feasibility of improving the keyhole stability to reduce and even avoid the formation of keyhole pores.

npj Computational Materials (2022)8:22; <https://doi.org/10.1038/s41524-022-00699-6>

INTRODUCTION

Metal additive manufacturing (AM) is well known for its ability to fabricate complex-shaped parts without special tooling¹ and functionally graded parts², shorten the development cycle of products³, and save the cost of the material⁴. However, the manufacturing defects^{4,5} are deleterious to the mechanical property. The porosity of the as-built part, one kind of defect, decreases the ultimate strength directly and is also a fatal flaw to the fatigue and fracture strength of the part^{6–8}. The presence of such defects does not meet the standards required in industry and thus prevents the adoption of AM technology in these industries. Therefore, massive research has been conducted to understand the pore formation mechanisms during AM and control the as-built part porosity^{8–13}. Among various pore defects, the porosity under the keyhole mode melting^{11,14} is a ubiquitous defect in both laser welding¹⁵ and laser powder bed fusion (L-PBF) and has attracted broad attention^{9,16,17}.

Some progress has been made on the study of the keyhole pore features, keyhole collapse mechanisms, and keyhole pore formation process. Ex situ experiments^{4,5,11} show that the keyhole pores are usually spherical and concentrate at the molten pool bottom. However, these experiments have not observed the keyhole pore formation directly, and cannot present quantitative explanations for the keyhole pore formation mechanisms. Recently, the in situ X-ray imaging of keyhole dynamics^{17–19} were presented, which identified three types of keyhole pores based on their positions: (i) the instant bubble by a ledge on the middle of the rear keyhole wall, which disappears rapidly during keyhole fluctuation, (ii) the keyhole pore at the end of the track due to laser stopping or turning around, and (iii) the keyhole pore at the bottom of the molten pool by the keyhole fluctuation. The first type of bubble is eliminated almost immediately after its formation and is insignificant for the pore formation mechanism. The pores at the end of the track¹⁸ are not only related to the keyhole dynamics but also determined by the laser scanning path, while these pores are usually reduced or eliminated by contour scanning and post-process polishing. Thus, the keyhole pore by the keyhole

fluctuation is the most significant, which is the focus of this study. The experiments by Zhao et al.¹⁹ and Cunningham et al.²⁰ suggested that the interaction between powder particles and laser in L-PBF only have second-order influence the keyhole fluctuation and keyhole pore formation. To exclude the influence of the randomly packed powder particles, the current study considers the bare plate only.

Besides the experimental approaches, numerical simulation of keyhole dynamics^{18,21–24} is a complementary, cost-saving and efficient approach to understand the formation mechanisms of the keyhole pores. Martin et al.¹⁸ simulated the keyhole pore at the end of the track and developed a strategy to reduce these pores. The simulation by Lin et al.²⁵ indicated that adjusting laser incident angle can reduce the number of keyhole pores during laser welding. Bayat et al.²⁶ investigated the relationship between the keyhole pores and input power, and validated the simulation results with the experiment results. The simulation by Tang et al.²⁷ indicated that the spherical pores at the bottom of the molten pool formed as the energy density increased during AM. The simulation by Tan et al.²⁸ showed the keyhole pore size decreased as the ambient pressure decreased.

Although the in situ experiments and previous simulations have provided empirical observations on the keyhole pore formation, the basic principles like the recoil pressure distribution on the keyhole surface, the relationship between energy distribution and keyhole fluctuation, and molten pool flow during the keyhole pore formation remain elusive. In this study, a multiphysics thermal-fluid flow model²⁴ incorporating heat transfer, molten pool flow, Marangoni effect, recoil pressure by metal evaporation, Darcy's law, and laser ray-tracing is adopted to simulate the keyhole fluctuation and keyhole pore formation process. Firstly, we validate the simulation results of instant bubble formation and pinning on the solidification front against the X-ray imaging results. Next, the varying trend of the keyhole depth fluctuation, absorbed energy distribution, keyhole pore size, molten pool flow, and forces on the keyhole with the increase of laser scanning speed are analyzed to explain the mechanisms and influence

¹Department of Mechanical Engineering, National University of Singapore, 117575 Singapore, Singapore. ✉email: mpeyanw@nus.edu.sg

factors of the keyhole pore formation. Furthermore, we explore the approach to reduce and even eliminate keyhole pores by simulating the molten pool flow under near-vacuum ambient pressure.

RESULTS AND DISCUSSION

Simulation setting

The laser parameters and ambient pressures in the simulation cases are listed in Supplementary Table 1, which are the same as the experiments¹⁹ except the Case 5 (the in situ experiment under low ambient pressure was not conducted). The laser spot size is 100 μm for all the simulations, the same as that in the experiments¹⁹. The physical properties of Ti-6Al-4V are listed in Supplementary Table 2. The mesh size is 4 μm to ensure numerical accuracy. To compare the keyhole pore features, the physical time of all the simulation cases is 2000 μs .

To rule out the influence of the powder particles, all the simulations are conducted on bare plates. However, the influence of the power bed on the keyhole pore formation still needs further study. Zhao et al.¹⁹ and Khairallah et al.²¹ showed that interactions between powder particles and laser ease the formation of keyhole pore. Moreover, the metal AM process under near-vacuum ambient by Tamas et al.²⁹ showed that the gas pores in the raw powders can be trapped in the molten pool and reside in the as-built part.

Based on our simulation results, the pore formation by keyhole collapse has two distinct stages: (i) the instant bubble formation due to the keyhole instability; (ii) the instant bubble pinning on the solidification front. The keyhole pore formation stages are validated by the X-ray imaging results¹⁹. Although the bubble can be formed due to the keyhole instability, both the simulation and experimental results show that the keyhole instability cannot ensure the instant bubble is captured by the solidification front and forming a pore in the scanning track.

Instant bubble due to the keyhole instability

Simulation Case 1 is to illustrate the instant bubble formation process due to the keyhole instability. According to the X-ray imaging results by Zhao et al.¹⁹, there are two different mechanisms for keyhole pore formation: pores driven by acoustic waves and pores by drag force. The acoustic wave is a fierce nonlinear phenomenon that cannot be simulated with the current model. Thus, this study focuses on the second type of keyhole pores mechanism. In both mechanisms found by¹⁹, an instant bubble appears first, where the keyhole shape experiences four stages: (i) A mini-keyhole protrudes on the top of the front keyhole wall with a letter "J" shape keyhole bottom; (ii) An instant bubble is formed with the keyhole collapse; (iii) A needle-like keyhole bottom (NKB) is formed as the keyhole drills down; (iv) The instant bubble moves away from the keyhole.

To illustrate the instant bubble formation by simulation, the mini-keyhole (protrusion) generation time is taken as the starting time point (Fig. 1a). The geometrical feature of the keyhole in the simulation is similar to that in the experimental results, as presented in Fig. 1d–f in time sequence. The depths of the newborn keyhole and NKB below the substrate in the experiment are about 99 and 226 μm , respectively, while they are 115 μm and 150 μm in the simulation as shown in Fig. 1e, f.

The velocity field of the molten pool to form the instant bubble is shown in Fig. 1d–f. In the 1st phase, the velocity around the middle of the rear keyhole (the rear and front parts are defined in Fig. 1g) is higher than other regions of the molten pool as shown in Fig. 1d. A protrusion, similar to the mini keyhole in Fig. 1a, on the front keyhole wall, is generated in Fig. 1d, and its velocity increases from the 1st phase to the 2nd phase (Fig. 1d and e) along the negative z direction so that it finally merges with the

rear keyhole wall to form the newborn keyhole. The high speed at the bottom of the newborn keyhole drives the keyhole penetration further to form a NKB in the 3rd phase as shown in Fig. 1f.

The distribution of the recoil pressure on the keyhole surface presented in Fig. 1g–i can further explain the instant bubble formation. To present the strong evaporation region on the keyhole surface, the region with the temperature above the boiling point (3315 K) is shown in Fig. 1j–l. It indicates that the evaporation on the keyhole surface is local. As the keyhole penetrates downward, the recoil pressure on the keyhole surface decreases (Fig. 1g), and the reverse flow pushes the rear keyhole wall forward (Fig. 1d). When the reverse flow is strong enough to break the balance of the rear keyhole wall, the keyhole would collapse like Fig. 1h. When the newborn keyhole forms, the evaporation is mainly concentrated at the bottom of the keyhole (Fig. 1k) and much higher than those in Fig. 1j and l. In this way, the keyhole is penetrating downward again driven by the recoil pressure. Thus, the decreasing recoil pressure and increasing reverse flow drive the rear keyhole collapse and recoil pressure is the main driving force for the keyhole penetration.

Zhao et al.¹⁹ proposed that in the 4th phase a shock wave by the phase explosion^{23,30} causes the keyhole tip to penetrate the instant bubble P_0 in the first mechanism for keyhole pore. The phase explosion is a fierce nonlinear process that occurs in less than 1 μs with "water hammer" pressure on instant bubble P_0 at ~ 140 MPa, which cannot be simulated with the current model. More importantly, the shock wave is not the decisive factor for the pinning of the bubble at the solidification front to form the keyhole pore. As the instant bubble is nearly stationary after its formation, the shock wave triggers and splits the bubble into two, which subsequently escapes to the surface of the molten pool in the X-ray experiment. Hence, no keyhole pore forms when a shock wave is encountered¹⁹. Therefore, more simulation cases are conducted to investigate how the instant bubble pins on the solidification front eventually form the keyhole pores.

Before further discussion of the keyhole pore formation, the issue below should be clarified. In the simulation, there is a keyhole pore with a diameter of 45 μm by two merged bubbles as shown in Fig. 1f, while there is no keyhole pore in the experiment¹⁹. There could be several reasons for this difference. The experimental results by Zhao et al.¹⁹ show that the laser parameters in Case 1 are close to the threshold for no keyhole pore, where the possibility of the keyhole pore formation is around zero. Meanwhile, the diameter of the laser in the experiment is an approximate value, and the influence of laser defocusing and plasma are not incorporated in the simulations. Thus, this kind of random error is acceptable.

Keyhole pore formation

According to the experimental results¹⁹, instant bubbles pin on the solidification front and form the keyhole pores under the manufacturing parameters in Case 2–4. The simulation result of Case 2 is taken as an example to explain the keyhole pore formation process, and the velocity distribution in the molten pool during the keyhole pore formation is shown in Fig. 2a–e. In Fig. 2a and b, the instant bubble b is formed as explained in section Instant bubble due to the keyhole instability. A protrusion is formed on the front keyhole wall as shown in the black dashed circle of Fig. 2a, and an instant bubble b is generated by the keyhole collapse in Fig. 2b. It takes about 240 μs for the instant bubble b to be pinned on the solidification front (Fig. 2e).

The liquid velocity distribution in the molten pool also changes during the bubble formation process. Generally, the liquid velocity at the front keyhole zone and rear-top region is higher than other regions in the molten pool and decreases with the distance to the rear keyhole (Fig. 1a) like the X-ray imaging results by Guo et al.³¹. However, the liquid velocity at the bottom region increases

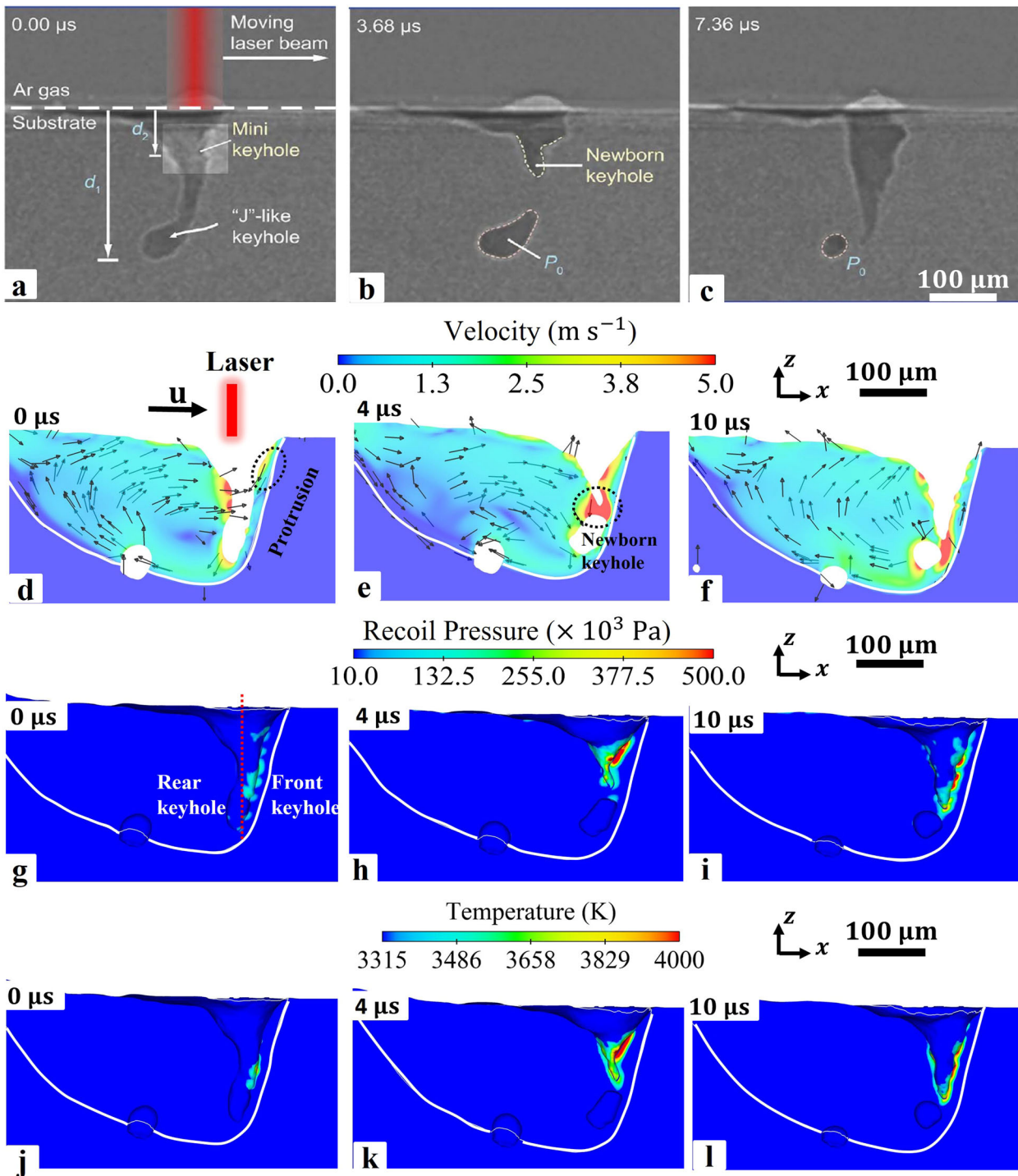


Fig. 1 Instant bubble formation due to the keyhole instability¹⁹. **a–c** is the X-ray imaging results of the keyhole instability¹⁹. **d–f**, **g–i**, and **j–l** are the velocity, recoil pressure, and keyhole surface temperature in the simulation Case 1. The laser position and scanning direction are indicated in **a** and **d**. The arrows in series **b** represent the velocity directions. The black dashed circle in **d** shows the protrusion on the front keyhole wall. The black dashed circle in **e** shows the newborn keyhole. The red dashed line in **g** represents the laser position and separates the keyhole as rear and front parts. The white solid lines in **b–l** are the contour of the solidus temperature T_s . The boiling temperature of Ti-6Al-4V is 3315 K under common ambient pressure, and **j–l** show the boiling region on the keyhole surface. (Experimental figures are from ref. ¹⁹, reprint with permission from AAAS).

sharply during the instant bubble formation stage as shown in Fig. 2a, b, and d. This could be the reason that keyhole shape changes, leading to the laser energy concentration at the bottom of the keyhole, which generates larger recoil pressure to push the liquid down as investigated by Zhao et al.²³. Due to the Bernoulli

effect, the liquid velocity between the bubble and the bottom of the molten pool is also higher.

The bubble motion and pore formation at the bottom of the molten pool in both the experiment and simulation are similar during the instant bubble pinning stage. The bubble *b* mainly

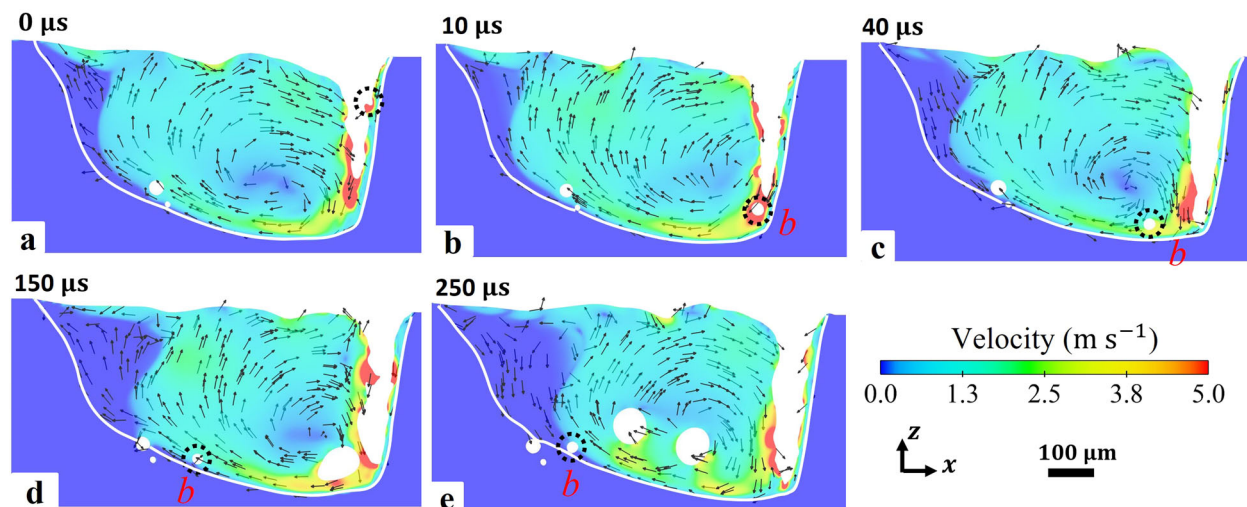


Fig. 2 The velocity field in the molten pool during the keyhole pore formation in Case 2. The black dashed circle in **a** is the mini keyhole. The bubble **b** in **b–e** is the instant bubble by the keyhole collapse. The white solid lines in **a–e** are the contour of the solidus temperature T_s .

moves along the horizontal direction without floating up as shown in Fig. 2c and d, similar to the experimental result¹⁹. About 20–30 μs after the keyhole collapse, the horizontal distance between the bubble **b** and the keyhole bottom is about 112 μm and 129 μm in the simulation and experiment, respectively. Furthermore, by observing the velocity distribution around the instant bubble **b**, we find that the liquid velocity below the bubble is much higher than that above in Fig. 2c. Based on Bernoulli's principle, the high velocity below the pore leads to low local pressure, which impedes the upward motion of the bubble. Eventually, the bubble is caught up by the solidification front. Thus, the velocity distribution at the bottom of the molten is one of the factors for the formation of the keyhole pore. This phenomenon also explains larger bubbles bear larger buoyancy and thus float up from the molten pool bottom with less hindrance in Fig. 2e.

Additionally, the drag force in the mushy zone is acting on the fluctuating keyhole, especially at the keyhole bottom. The influence of mushy zone on keyhole dynamics and keyhole pore formation is further discussed in Supplementary Note 2. Based on the analysis of the instant bubble formation and pinning on solidification front stages, the schematic of the keyhole pore formation is presented in Fig. 3. With the unbalanced forces, the keyhole fluctuates up and down and even collapses to form instant bubbles (b_1 and b_2). In the bubble pinning on solidification front stage, the molten pool bottom has a higher velocity than that above the bubble b_1 and lower pressure, which leads to a vertical drag force on the bubble b_1 . If the drag force is sufficiently strong, the bubble b_1 would move nearly horizontally and pins on the solidification front like b_2 .

Keyhole pore feature

The keyhole and keyhole pore features in simulation Case 2–4 are presented in Fig. 4 and listed in Table 1. The maximum keyhole pore sizes in both simulation and experiment decrease as the laser scanning speed decreases (with the same laser power). At low scanning speeds, the maximum keyhole pore sizes in simulation and experiment are close to each other with differences lower than 4 μm as shown in Fig. 4d. When the laser scanning speed reaches the threshold for no keyhole pore (Case 2), the contingency of the maximum keyhole pore size increases. In simulation Case 2, the bubble b_1 (size of 76 μm) is pinned on the solidification front, while the similar bubble b_1^* (size of 80 μm) floats up to the molten pool surface. Nonetheless, the size of the

second maximum keyhole pore b_1' is 36 μm and close to the experimental result of 18 μm . It should be mentioned that the keyhole pore size is sensitive to the experimental parameters near the threshold for no keyhole pore situations, such as the laser focusing and defocusing, material purity, and laser deflection of the vapor plume, etc. While the current simulation model cannot incorporate all the influence factors, the difference of maximum keyhole pore size in Case 2 is acceptable. Since the maximum keyhole pore size has certain randomness in both simulation and experiment, other parameters, such as mean keyhole pore size, the median value of pore size, and pore distribution, would be more representative, but were not provided by the experiment¹⁹. The mean keyhole pore size in the simulations increases steadily as the laser scanning speed decreases (Table 1).

The keyhole pores are concentrated at the bottom of the laser scanning track with smooth surfaces compared to the lack-of-fusion pores. Further observation of the keyhole pore distribution in Fig. 4a–c shows that not only does the keyhole pore size increase sharply as the laser scanning speed decreases but also the position and shape of the pores change. In Case 2, the keyhole pores are spherical and horizontally distributed in the laser scanning track. As the laser scanning speed decreases, the shape of the keyhole pores becomes increasingly irregular with a flat or sharp bottom, while the upper surface remains smooth and spherical. Additionally, the different sizes of the instant bubbles in the low scanning speed cases also lead to different buoyant forces, vertical motions to a certain degree and thus the non-horizontal distribution of the pores.

As the instant bubble formation is related to the keyhole collapse, the statistical features of the keyhole depth are given in Fig. 4e, f and Table 1. The mean keyhole depths in the simulation cases match those in the experiments (Fig. 4e), although the relative difference of the keyhole depth between the simulations and experiments increases from 2.5 to 15% as the laser scanning speed decreases. This diverging discrepancy can be explained by several reasons. Firstly, the aforementioned bulk explosion is fiercer as the energy density increases. Next, the plume in a deeper keyhole traps more photons, leading to greater energy absorptivity in the material. This effect is not considered in the current model. Additionally, the laser diameter varies along with the keyhole depth due to defocusing, which influences the laser reflections and energy absorption. In the welding process, the experiments by Li et al.³² showed that the keyhole depth and laser absorptivity increase as the distance between the laser focal point and substrate increases when the focal point is below the

substrate. Without exact data about laser energy distribution in the experiment, the laser in the current model is assumed to be parallel with a constant diameter instead. The influence of laser

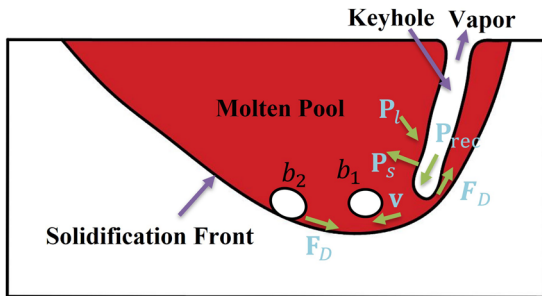


Fig. 3 Schematic of the keyhole pore formation process. The recoil pressure (P_{rec}) by metal evaporation, hydrodynamic pressure (P_l), pressure by surface tension (P_s), and drag force in the mushy zone (F_D) lead to the instability of the keyhole and generate bubbles b_1 and b_2 . The bubbles are not floating up directly due to Bernoulli's principle and are caught by the solidification front.

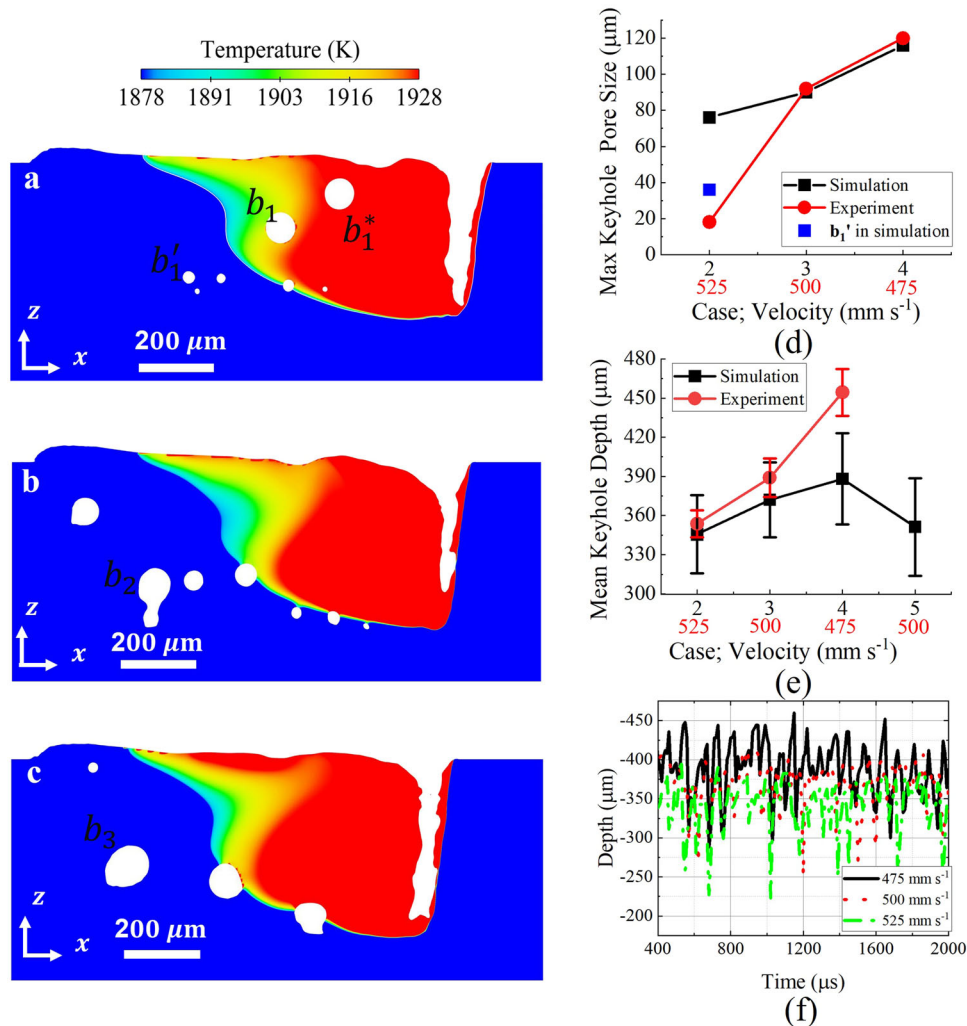


Fig. 4 Keyhole and keyhole pore features. **a–c** Keyhole pores in Case 2 (525 mm.s^{-1}), Case 3 (500 mm.s^{-1}), and Case 4 (475 mm.s^{-1}) in the center plane of the scanning track at $t = 2000 \mu\text{s}$. **d, e** Maximum keyhole pore size and mean keyhole depth between simulation and experiment. **f** Keyhole depth fluctuation with time. b_1 , b_2 , and b_3 are the maximum pore in Case 2–4, respectively. b_1' in **a** is the second largest pore in simulation Case 2, indicated in **e**. The case number and laser scanning speed are shown in **d, e** together for better comparison. The error bars in **e** are the standard deviation of the keyhole depths.

defocusing needs further study to improve the accuracy of the model.

As the laser scanning speed decreases, the keyhole depth curves in Fig. 4f show an obvious increase, similar to the increasing trend of mean keyhole pore size. Moreover, the standard deviation of the keyhole depth in Case 4 is obviously larger than those Case 2 and 3 in Table 1, which indicates that the keyhole fluctuation in Case 4 is much more violent. The standard deviation of keyhole depth in the experiment is smaller than that in the simulation might be because the sampling interval in the experiment (around $20 \mu\text{s}$) is larger than that in the simulation ($1 \mu\text{s}$). The sampling interval in experiments is larger than the instant bubble formation duration (around $7 \mu\text{s}$), which results in the difference of the standard deviation. Compared to the mean keyhole depth, the maximum fluctuations of keyhole depth in three cases are larger than 40% of the mean keyhole depth. The analysis of section Instant bubble due to the keyhole instability indicates that the higher keyhole depth variation between the 1st phase and the 2nd phase makes the keyhole more unstable and generates instant bubbles more easily. Thus, there is a higher probability of the keyhole pore formation in Case 4. Additionally, the X-ray imaging results^{17,19} also show that the shallow keyhole with a large keyhole fluctuation distance can lead to pores,

Table 1. Statistical features of keyhole pore size, depth, and simulate energy absorptivity.

		Case 2	Case 3	Case 4	Case 5
Mean keyhole depth (μm)	Exp. ^a	355	388	456	–
	Sim. ^b	345	372	388	351
Mean keyhole pore size ^c (μm)		37	49	82	–
s.d. ^d of keyhole depth (μm)	Exp. ^a	10	14	17	–
	Sim. ^b	30	29	35	37
Maximum fluctuation of keyhole depth ^e (μm)		152	170	156	164
Absorptivity on front keyhole wall	Mean (%)	25.54	26.07	27.07	25.58
	s.d. ^d (%)	2.29	2.51	2.63	2.23
Absorptivity on rear keyhole wall	Mean (%)	50.04	49.88	49.04	50.40
	s.d. ^d (%)	3.02	3.26	4.21	2.75

^aExp. represents the experiment result.
^bSim. represents the simulation result.
^cThe pores in the solidified region are considered.
^ds.d. means standard deviation.
^eIt is the distance from the peak to the valley of keyhole depth curves.

especially in the case of laser scanning the powder bed (the spattering particles influence laser absorption and metal vapor flow). It suggests that the keyhole depth and its fluctuation are two important parameters for keyhole pore formation and should be considered for future observations and analysis.

The velocity magnitudes and streamlines of the Case 2–4 share similar distributions as plotted in Fig. 5. The velocity magnitude is larger around the keyhole and molten pool bottom than in other regions. The streamline distributions in Fig. 5d–f show that there are two vortices in the molten pool: a larger stronger clockwise vortex at the front part of the molten pool and a smaller weaker anticlockwise vortex at the rear part of the molten pool. The distribution and location of the vortex pair match well with those observed in the X-ray imaging experiments by Hojjatzadeh et al.³³. As the keyhole pores always form at the bottom of the melt track, the velocity distribution at the bottom of the melt pool is more relevant and influential. At the molten pool bottom, the liquid flows horizontally to the rear part of the molten pool and thus drives the instant bubble backwards to the solidification front.

Although the fluctuation of total recoil force in Case 2–4 is similar as shown in Supplementary Fig. 3, the analysis of the energy absorptivity in the three cases hints at the relationship between the keyhole pore formation and keyhole dynamics. The total energy absorptivity and that on the rear keyhole wall are different from that on the front keyhole wall (Fig. 6). In simulation Case 4, the total energy absorptivity and that on the rear keyhole wall have fiercer fluctuations compared to that on the front keyhole wall. As the laser reflection is determined by the morphology of the keyhole, it indicates that the shape variation of the rear keyhole wall is larger in Case 4. The mean value and standard deviation of the absorptivity are listed in Table 1. While the mean absorptivity on each part of the keyhole surface is similar in the three cases, the standard deviation on the rear keyhole wall increases as the scanning speed decreases. This observation implies that the keyhole morphology is sensitive to the laser scanning speed, especially the rear keyhole wall, which is closely related to the keyhole fluctuation and instant bubble formation. In other words, the energy absorptivity fluctuation could be an effective criterion to evaluate the possibility of the

keyhole pore formation. It should be specified that the absorbed energy includes the energy absorbed by the melted and unmelted regions together. Since the laser diameter has not been precisely measured in the experiments by Argonne National Lab and the shape of the melted region is changing during the laser scanning, the exact energy absorbed by the melted and unmelted region is not distinguished currently. In the future, experiment and simulation data of energy absorbed by the melted and unmelted regions may be useful to better predict the possibility of keyhole pore formation.

The above analysis of the keyhole pore features in Case 2–4 shows that the keyhole pore size is sensitive to the manufacturing parameters. The increase of laser scanning speed is $50 \text{ mm}\cdot\text{s}^{-1}$, while the mean keyhole pore size decreases from 82 to $37 \mu\text{m}$. While the molten pool flow of the cases is similar, the deviation of keyhole depth and energy absorptivity fluctuation reflects the keyhole instability.

Reduce keyhole pores: low ambient pressure

The mechanisms of keyhole pore formation as discussed above shows that the balance of the forces on the keyhole surface is important to ameliorate the pores formed by keyhole fluctuation. Although it has been proven that the porosity of the as-built part under near-vacuum and low ambient pressure can be reduced during both AM and laser welding^{34–36}, the principles on how the ambient environment influences the keyhole and molten pool dynamics and reduce the pores during AM are rarely studied yet. To explore the principles of using low ambient pressure to reduce keyhole pores, a simulation (Case 5) is conducted under 10^{-4} atm , in which the other manufacturing parameters are kept the same as Case 3.

As presented in Fig. 7, there are no keyhole pores in the simulation domain in Case 5. The decreasing trend of pore formation under low ambient pressure in the simulation is similar to the experiments^{35,37}, where there are nearly no pores under the ambient pressure below 100 Pa. The temperature, velocity distribution, and streamline in Case 5 are similar to those in Case 3. Despite the decrease in ambient pressure, the molten pool shapes are similar, and the depth increases slightly from 416 to $430 \mu\text{m}$. A vortex pair is observed, with a larger and stronger clockwise rotating vortex at the front part of the molten pool. At the bottom region, the velocity decreases longitudinally from the front to the rear end of the molten pool.

The main differences between Case 3 and 5 are the ambient pressure and consequently the recoil pressure. The keyhole fluctuation is dynamic, and the recoil pressure changes with the ambient pressure and keyhole surface temperature. Thus, further analysis of the recoil pressure on the keyhole surface is necessary as given in Fig. 8. Calculated by our evaporation model²⁴, the recoil pressure-surface temperature curves under different ambient pressures are different as shown in Supplementary Fig. 4. Although the amplitude of the recoil pressure at high temperature is similar, the boiling temperature decreases as the ambient pressure drops. Therefore, the temperature and recoil pressure ranges in Fig. 8 for the two cases are different.

In Case 3, the region near the keyhole with the temperature above the boiling point is small and randomly distributed on the front keyhole wall (Fig. 8a). Correspondingly, the recoil pressure is concentrated on the front keyhole wall (Fig. 8c). Thus, the rear keyhole wall has weak support from the recoil pressure and collapses easily to form instant bubbles. In contrast, the recoil pressure distribution under the low ambient pressure is different. Although the highest temperature on the keyhole surface in Fig. 8b is close to that in Fig. 8a at around 4000 K, the temperature of nearly the entire keyhole surface is above the boiling temperature and the temperature increases continuously from the upper to the bottom region of the keyhole. This temperature distribution

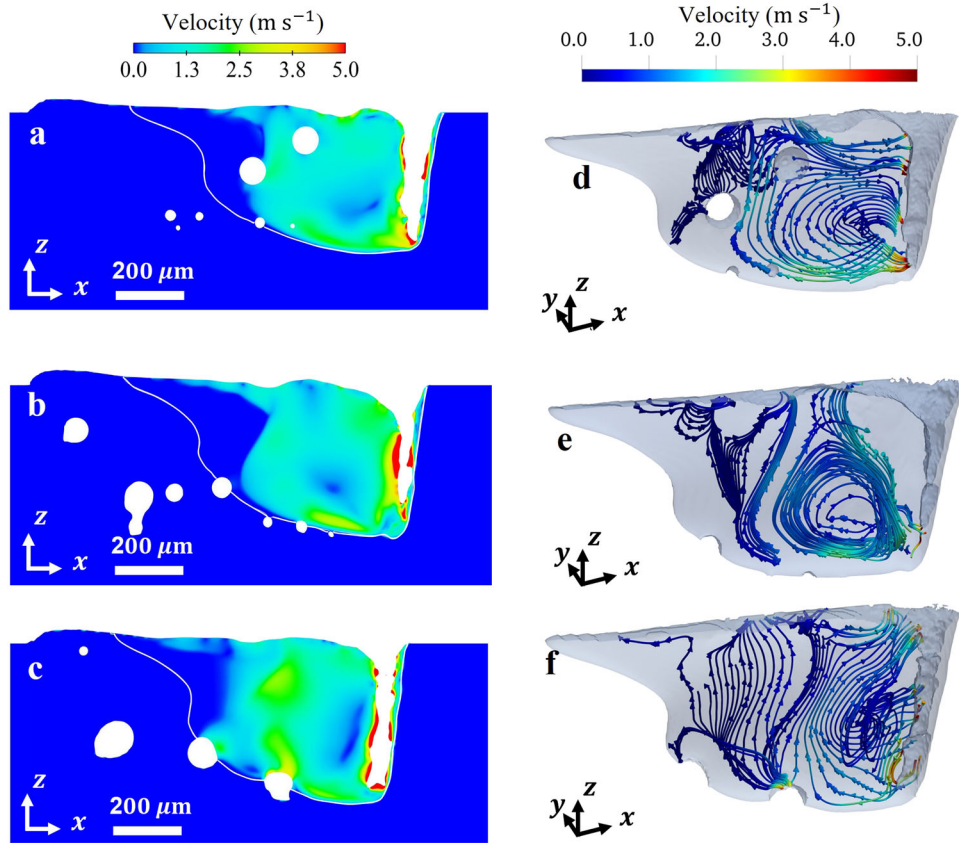


Fig. 5 Velocity field of the molten pool in Case 2–4. **a–c** Velocity magnitude and **d–f** streamline in the molten pool at $t = 2000 \mu\text{s}$ in Case 2 (**a, d**), Case 3 (**b, e**), and Case 4 (**c, f**). The white solid curves in **a–c** and gray contours in **d–f** are the contour of the solidus temperature T_s .

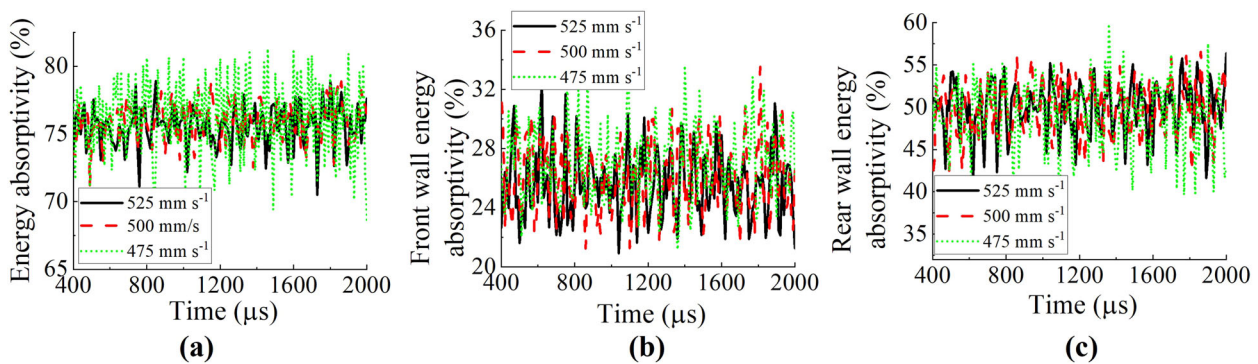


Fig. 6 Energy absorptivity on the keyhole surface in Case 2–4. **a** The whole keyhole surface, **b** front keyhole wall, and **c** rear keyhole wall.

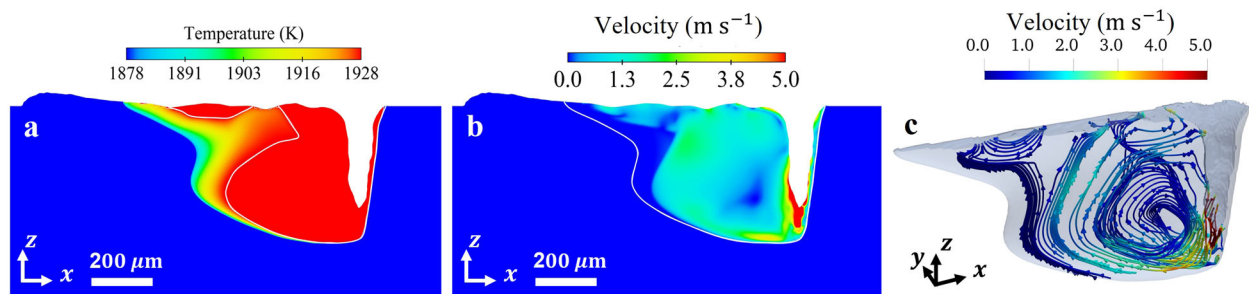


Fig. 7 Simulation results of the molten pool flow under 10^{-4} atm ambient pressure (Case 5) at $t = 2000 \mu\text{s}$. **a** Temperature distribution, **b** velocity magnitude distribution, and **c** streamline in the molten pool. The white curve in **a** is the contour of the liquidus temperature T_l , and the white curve in **b** and gray contour in **c** are the contour of the solidus temperature T_s .

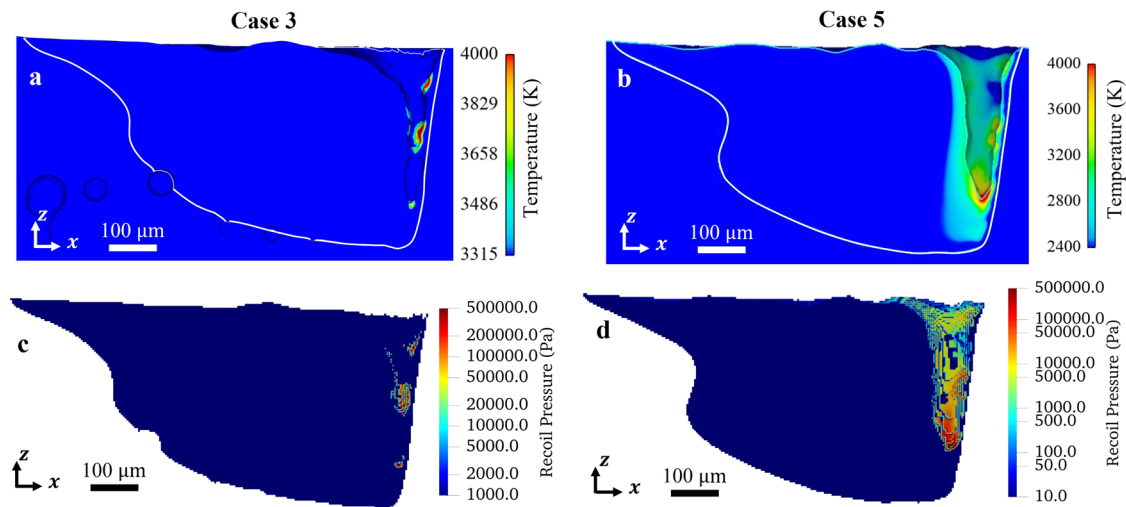


Fig. 8 Comparison of temperature and recoil pressure on the keyhole surface under different ambient pressure. **a, b** Temperature field above the boiling temperatures and **c, d** recoil pressure on the keyhole surface under the common ambient (Case 3) and low ambient pressure (Case 5). **a, c** and **b, d** are the simulation results of Case 3 and 5, respectively. The white curves in **a** and **b** are the contour of the solidus temperature T_s .

indicates stronger evaporation from the keyhole surface under the low ambient pressure, which follows the trend in previous experiments^{35,38}. Moreover, the recoil pressure on the keyhole surface is distributed all over the keyhole surface with a value above 0.1 atm and up to 5 atm at the bottom of the keyhole. Compared to the recoil pressure distribution in Case 3 (Fig. 8c), the recoil pressure on the rear keyhole wall under the low ambient pressure is higher which stabilizes the rear keyhole wall during fluctuation and thus reduces keyhole pores.

To further analyze the stability of the keyhole under different ambient pressures, the keyhole depth and energy absorptivity of Case 3 and 5 are given in Fig. 9. The keyhole depth in Case 5 fluctuates more violently than that in Case 3. The standard deviation of keyhole depth in Case 5 is 37 μm , about 28% higher than that in Case 3 as listed in Table 1. However, the keyhole depth is not indicative of the keyhole instability under the low ambient pressure. Further analysis of the energy absorptivity on keyhole surface from Fig. 9b–d and Table 1 shows that the absorptivity fluctuations trend under different ambient pressures are similar to each other, whereas the standard deviations of the energy absorptivity on both the front and rear keyhole wall in Case 5 are lower than those in Case 3 and even lower than those in Case 2. As analyzed in section Keyhole pore feature, the keyhole stability is sensitive to the manufacturing parameters, which also explains why there is no keyhole pore in Case 5. The energy absorption is calculated via the ray-tracing method, which is largely determined by the geometric shape of the keyhole. Therefore, the lower standard deviation of the energy absorptivity is indicative of a smaller distortion of the keyhole shape, especially the rear keyhole wall.

Furthermore, the similar energy absorptivity on the rear keyhole wall under the low ambient leads to higher evaporation and higher recoil pressure than that under common ambient pressure. The analysis above indicates that the keyhole depth fluctuation is more volatile under low ambient pressures because the evaporation is greater compared to that under common ambient pressure. Simultaneously, the recoil pressure on the rear keyhole wall increases to maintain the stability of the keyhole shape. Thus, the keyhole is stabler under low ambient pressure to reduce the porosity in the keyhole melting mode.

Since the keyhole depth increases as the ambient pressure decrease, a lower laser energy density can achieve a similar

molten pool shape. Additionally, metal AM experiments^{38,39} under low ambient encounter another problem: the evaporation mass loss of elements like Aluminum, Magnesium, and Manganese in alloys increases and influences the element concentration and the crystal phase of the final part. To control the grain structure, the element concentration of the raw material should be adjusted.

In summary, keyhole pore formation during metal additive manufacturing has been investigated in this work with a multi-physics thermal-fluid flow model, and directly validated with the X-ray imaging results. The following conclusions can be drawn:

- (1) The keyhole pore formation process has two distinct stages: (i) the instant bubble formation and (ii) pinning on the solidification front stage. The instant bubble formation is mainly due to the keyhole instability (unbalanced forces on the rear keyhole wall). During the bubble pinning on the solidification front, the high flow speed below the instant bubble generates a vertical drag force which impedes the bubble from floating up to the molten pool surface. The bubble is finally caught by the solidification front to form the keyhole pore.
- (2) The unevenly distributed recoil pressure on the keyhole surface increases the possibility of keyhole collapse to form keyhole pores. Additionally, the drag force from the mushy zone is pertinent as it determines the keyhole fluctuation at the bottom of the melt pool. A Darcy drag force model with the consideration of grain morphology in AM is required to improve the accuracy of drag force and keyhole fluctuation calculation.
- (3) The keyhole pore size is sensitive to the manufacturing parameters. As the laser scanning speed slightly increases, the keyhole pore sizes decrease significantly, and the shape of the keyhole pore becomes spherical and horizontally distributed at the molten pool bottom. Moreover, the features of keyhole fluctuation and energy absorptivity variation could be criterions to predict the likelihood of keyhole pore formation.
- (4) Low ambient pressure is a feasible way to reduce or even eliminate the formation of keyhole pores. Compared to the common ambient pressure, the recoil pressure on the rear keyhole wall under low ambient is larger and maintains a stable keyhole shape.

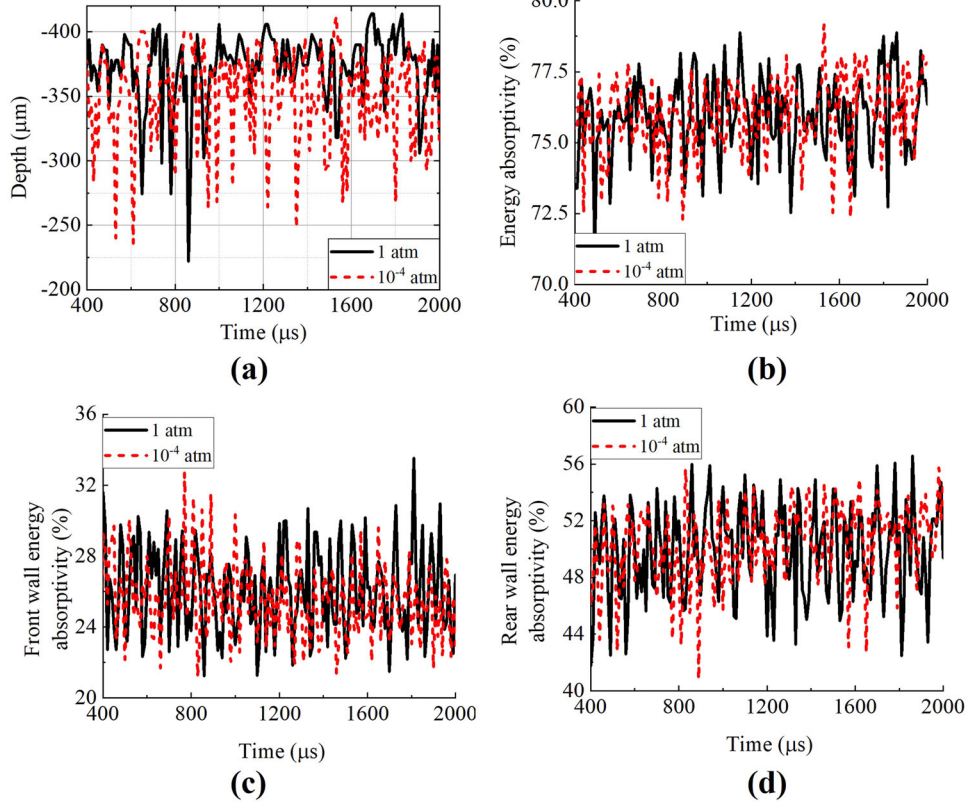


Fig. 9 Keyhole depth and energy absorptivity in Case 3 (1 atm) and Case 5 (10⁻⁴ atm). **a** Keyhole depth, **b** total energy absorptivity, **c** energy absorptivity on the front keyhole wall, and **d** energy absorptivity on the rear keyhole wall.

METHODS

Multiphysics thermal-fluid flow model

Different from the ALE3D code used by Khairallah et al.²² and Finite Element Method (FEM) used by Zhu et al.⁴⁰, a multiphysics thermal-fluid flow model based on the Finite Volume Method is adopted in the current study. This model is mainly based on our previous work^{24,41}, where the drag force in the mush zone is modified according to the Blake-Kozeny model. Because the in situ experiment by Zhao et al.¹⁹ suggested that the drag force has an effect on the keyhole pore formation. In the model, the liquid phase is assumed to be incompressible Newtonian fluid with laminar flow. The mass conservation equation is given as follows:

$$\nabla \cdot (\rho \mathbf{v}) = 0 \quad (1)$$

where ρ and \mathbf{v} are the mass density and velocity vector.

The momentum conservation equation is given as follows:

$$\rho \frac{\partial \mathbf{v}}{\partial t} + \rho \nabla \cdot (\mathbf{v} \otimes \mathbf{v}) = -\nabla p + \mu \nabla^2 \mathbf{v} + \mathbf{f}_b - \rho D \mathbf{v} \quad (2)$$

where μ and p denote the dynamic viscosity and pressure. The buoyancy force \mathbf{f}_b is accounted for using the Boussinesq approximation

$$\mathbf{f}_b = \rho \mathbf{g} \alpha_v (T - T_{\text{ref}}) \quad (3)$$

where \mathbf{g} , α_v , and T_{ref} denote the gravitational acceleration vector, the thermal expansion coefficient, and reference temperature (liquidus temperature T_l for the current simulation).

In the molten pool, the liquid velocity decreases sharply in the mushy zone due to the drag force by the grain structure. To describe the drag force in the mushy zone, there are usually two ways, temperature-dependent viscosity and Darcy drag force, applied to the fluid flow model. Since the time step size decreases sharply with higher viscosity ($\mu > 0.01$ Pa.s), the experiment-based Darcy drag force model, Blake-Kozeny model^{42,43}, is implemented in the current model. D is the Darcy drag

force coefficient, which is given as

$$D = \frac{180\mu}{\rho \lambda_1^2} \frac{F_s^2}{(1 - F_s)^3} \quad (4)$$

where λ_1 is the characteristic length of mushy zone, taken as the primary dendrite arm spacing (about 5 μm for SLM⁴⁴), and $\frac{180\mu}{\rho \lambda_1^2} = 5.57 \times 10^6$ in the current study. F_s is the solid fraction. Further analysis of the influence of Darcy drag on molten pool flow and keyhole pores distribution are given in Supplementary Note 2.

The energy conservation equation is given as follows:

$$\rho \frac{\partial l}{\partial t} + \rho \nabla \cdot (\mathbf{v} l) = \nabla \cdot (k \nabla T) + q \quad (5)$$

where k is the thermal conductivity, and T is the temperature. $l = \int C_p dT + (1 - F_s)L_m$ is the specific internal energy, where C_p and L_m are the specific heat and specific latent heat of melting. q is the power absorbed by the material, which is incorporated by using the ray-tracing method⁴⁵ to track the multireflections of laser and calculated with the Fresnel equation. In the current model, the reflection is assumed to be a specular reflection. The material for simulation in the current work is Ti-6Al-4V, but titanium's⁴⁶ complex refractive index is used instead due to the lack of reliable data of Ti-6Al-4V.

The free surface of the molten pool is captured using the volume-of-fluid (VoF) method⁴⁷.

$$\frac{\partial F}{\partial t} + \nabla \cdot (F \mathbf{v}) = 0 \quad (6)$$

where F is the volume fraction.

On the free surface, the normal (p_n) and tangent forces (τ_t) incorporate the surface tension, recoil pressure and Marangoni effect, given as

$$\begin{cases} p_n = \sigma(T)\kappa + P_{\text{rec}}(T) \\ \tau_t = \sigma'_T [\nabla T - \mathbf{n}(\nabla T \cdot \mathbf{n})] \end{cases} \quad (7)$$

where κ is the curvature of the free surface, and \mathbf{n} is the normal vector of the free surface. $\sigma(T) = \sigma_0 - \sigma'_T (T - T_l)$. σ_0 and σ'_T are surface tension coefficient at the reference temperature T_l (liquidus temperature in the

current simulations) and its temperature sensitivity. $P_{\text{rec}}(T)$ is the recoil pressure²⁴. Both surface tension, recoil pressure, and Marangoni effect are treated as boundary conditions.

For the thermal boundary condition²⁶, it consists of heat convection, heat radiation, and heat loss of evaporation

$$-k\nabla T \cdot \mathbf{n} = h(T - T_{\text{env}}) + c\sigma_s(T^4 - T_{\text{env}}^4) + \dot{q}_{\text{evp}} \quad (8)$$

where σ_s and T_{env} are the Stefan-Boltzmann constant ($5.6704 \times 10^{-8} \text{ W m}^{-2} \text{ K}^{-4}$) and the ambient temperature, respectively. $\dot{q}_{\text{evp}} = \dot{m}_{\text{evp}}l$ is the heat loss rate by evaporation, where \dot{m}_{evp} is the mass-loss rate by evaporation and calculated with our previous evaporation model²⁴.

Since the density of the liquid is more than 1000 times larger than gas, above the free surface, the ideal gas equation is applied for the void region ($p_g V_g^\gamma$ is constant, where p_g , V_g , γ are the gas pressure, gas volume, and the ratio of specific heat for the gas). After the instant bubble formed (gas trapped by the liquid), the bubble is taken as adiabatic, which means there is no heat transfer between bubble and liquid, and the pressure in the bubble is dependent on the volume of the bubble

$$p = p_0 \left(\frac{V_0}{V} \right)^\gamma \quad (9)$$

where (p_0, V_0) is the state when the bubble is formed.

DATA AVAILABILITY

The main data supporting the finding of this study are available within the article. Extra data are available from the corresponding author upon reasonable request.

Received: 13 September 2021; Accepted: 23 December 2021;

Published online: 27 January 2022

REFERENCES

- Yang, L., Harrysson, O., West, H. & Cormier, D. Compressive properties of Ti-6Al-4V auxetic mesh structures made by electron beam melting. *Acta Mater.* **60**, 3370–3379 (2012).
- Yan, W. et al. Multi-scale modeling of electron beam melting of functionally graded materials. *Acta Mater.* **115**, 403–412 (2016).
- Wei, H. et al. Mechanistic models for additive manufacturing of metallic components. *Prog. Mater. Sci.* **116**, 100703 (2021).
- DebRoy, T. et al. Additive manufacturing of metallic components—process, structure and properties. *Prog. Mater. Sci.* **92**, 112–224 (2018).
- Snow, Z., Nassar, A. & Reutzel, E. W. Review of the formation and impact of flaws in powder bed fusion additive manufacturing. *Addit. Manuf.* **36**, 101457 <https://www.sciencedirect.com/science/article/pii/S2214860420308290>, <https://doi.org/10.1016/j.addma.2020.101457> (2020).
- Beretta, S. & Romano, S. A comparison of fatigue strength sensitivity to defects for materials manufactured by am or traditional processes. *Int. J. Fatigue* **94**, 178–191 (2017).
- Masuo, H. et al. Influence of defects, surface roughness and hip on the fatigue strength of ti-6al-4v manufactured by additive manufacturing. *Int. J. Fatigue* **117**, 163–179 (2018).
- Yang, K. V. et al. Porosity formation mechanisms and fatigue response in al-sim alloys made by selective laser melting. *Mater. Sci. Eng. A* **712**, 166–174 (2018).
- Aboulkhair, N. T., Everitt, N. M., Ashcroft, I. & Tuck, C. Reducing porosity in als10mg parts processed by selective laser melting. *Addit. Manuf.* **1**, 77–86 (2014).
- Weingarten, C. et al. Formation and reduction of hydrogen porosity during selective laser melting of als10mg. *J. Mater. Process. Technol.* **221**, 112–120 (2015).
- King, W. E. et al. Observation of keyhole-mode laser melting in laser powder-bed fusion additive manufacturing. *J. Mater. Process. Technol.* **214**, 2915–2925 (2014).
- Leung, C. L. A. et al. The effect of powder oxidation on defect formation in laser additive manufacturing. *Acta Mater.* **166**, 294–305 (2019).
- Yang, T. et al. Laser powder bed fusion of als10mg: Influence of energy intensities on spatter and porosity evolution, microstructure and mechanical properties. *J. Alloy. Compd.* **849**, 156300 (2020).
- Cunningham, R., Narra, S. P., Montgomery, C., Beuth, J. & Rollett, A. Synchrotron-based x-ray microtomography characterization of the effect of processing variables on porosity formation in laser power-bed additive manufacturing of ti-6al-4v. *JOM* **69**, 479–484 (2017).
- Fabbro, R. Melt pool and keyhole behaviour analysis for deep penetration laser welding. *J. Phys. D Appl. Phys.* **43**, 445501 (2010).
- Forien, J.-B. et al. Detecting keyhole pore defects and monitoring process signatures during laser powder bed fusion: a correlation between in situ pyrometry and ex situ x-ray radiography. *Addit. Manuf.* **35**, 101336 (2020).
- Hojjatzadeh, S. M. H. et al. Direct observation of pore formation mechanisms during lpbfd additive manufacturing process and high energy density laser welding. *Int. J. Mach. Tools Manuf.* **153**, 103555 (2020).
- Martin, A. A. et al. Dynamics of pore formation during laser powder bed fusion additive manufacturing. *Nat. Commun.* **10**, 1987 (2019).
- Zhao, C. et al. Critical instability at moving keyhole tip generates porosity in laser melting. *Science* **370**, 1080–1086 (2020).
- Cunningham, R. et al. Keyhole threshold and morphology in laser melting revealed by ultrahigh-speed x-ray imaging. *Science* **363**, 849–852 (2019).
- Khairallah, S. A., Anderson, A. T., Rubenchik, A. & King, W. E. Laser powder-bed fusion additive manufacturing: Physics of complex melt flow and formation mechanisms of pores, spatter, and denudation zones. *Acta Mater.* **108**, 36–45 (2016).
- Khairallah, S. A. et al. Controlling interdependent meso-nanosecond dynamics and defect generation in metal 3d printing. *Science* **368**, 660–665 (2020).
- Zhao, C. et al. Bulk-explosion-induced metal spattering during laser processing. *Phys. Rev. X* **9**, 021052 (2019).
- Wang, L., Zhang, Y. & Yan, W. Evaporation model for keyhole dynamics during additive manufacturing of metal. *Phys. Rev. Appl.* **14**, 064039 (2020).
- Lin, R., Wang, H.-p., Lu, F., Solomon, J. & Carlson, B. E. Numerical study of keyhole dynamics and keyhole-induced porosity formation in remote laser welding of al alloys. *Int. J. Heat. Mass Transf.* **108**, 244–256 (2017).
- Bayat, M. et al. Keyhole-induced porosities in Laser-based Powder Bed Fusion (L-PBF) of Ti6Al4V: high-fidelity modelling and experimental validation. *Addit. Manuf.* **30**, 100835 (2019).
- Tang, C., Tan, J. L. & Wong, C. H. A numerical investigation on the physical mechanisms of single track defects in selective laser melting. *Int. J. Heat. Mass Transf.* **126**, 957–968 (2018).
- Tan, P., Kiran, R. & Zhou, K. Effects of sub-atmospheric pressure on keyhole dynamics and porosity in products fabricated by selective laser melting. *J. Manuf. Process.* **64**, 816–827 (2021).
- Tammam-Williams, S., Withers, P. J., Todd, I. & Prangnell, P. Porosity regrowth during heat treatment of hot isostatically pressed additively manufactured titanium components. *Scr. Mater.* **122**, 72–76 (2016).
- Miotello, A. & Kelly, R. Laser-induced phase explosion: new physical problems when a condensed phase approaches the thermodynamic critical temperature. *Appl. Phys. A* **69**, S67–S73 (1999).
- Guo, Q. et al. In-situ full-field mapping of melt flow dynamics in laser metal additive manufacturing. *Addit. Manuf.* **31**, 100939 (2020).
- Li, S., Chen, G., Katayama, S. & Zhang, Y. Relationship between spatter formation and dynamic molten pool during high-power deep-penetration laser welding. *Appl. Surf. Sci.* **303**, 481–488 (2014).
- Hojjatzadeh, S. M. H. et al. Pore elimination mechanisms during 3D printing of metals. *Nat. Commun.* **10**, 3088 (2019).
- Zhang, B., Liao, H. & Coddet, C. Microstructure evolution and density behavior of cp ti parts elaborated by self-developed vacuum selective laser melting system. *Appl. Surf. Sci.* **279**, 310–316 (2013).
- Zhou, B., Zhou, J., Li, H. & Lin, F. A study of the microstructures and mechanical properties of ti6al4v fabricated by slm under vacuum. *Mater. Sci. Eng. A* **724**, 1–10 (2018).
- Jiang, M., Chen, X., Chen, Y. & Tao, W. Mitigation of porosity defects in fiber laser welding under low vacuum. *J. Mater. Process. Technol.* **276**, 116385 (2020).
- Katayama, S., Kobayashi, Y., Mizutani, M. & Matsunawa, A. Effect of vacuum on penetration and defects in laser welding. *J. Laser Appl.* **13**, 187–192 (2001).
- Zhou, J. et al. Research on aluminum component change and phase transformation of TiAl-based alloy in electron beam selective melting process under multiple scan. *Intermetallics* **113**, 106575 (2019).
- Tang, H. P. et al. Additive manufacturing of a high niobium-containing titanium aluminide alloy by selective electron beam melting. *Mater. Sci. Eng. A* **636**, 103–107 (2015).
- Zhu, Q. & Yan, J. A mixed interface-capturing/interface-tracking formulation for thermal multi-phase flows with emphasis on metal additive manufacturing processes. *Comput. Methods Appl. Mech. Eng.* **383**, 113910 (2021).
- Yan, W. et al. Multi-physics modeling of single/multiple-track defect mechanisms in electron beam selective melting. *Acta Mater.* **134**, 324–333 (2017).
- Poirier, D. R. Permeability for flow of interdendritic liquid in columnar-dendritic alloys. *Metall. Mater. Trans. B* **18**, 245–255 (1987).
- Amador, C. & de Juan, L. M. Strategies for structured particulate systems design. *Comput. Aided Chem. Eng.* **39**, 509–579 (2016).

44. Wang, Y. M. et al. Additively manufactured hierarchical stainless steels with high strength and ductility. *Nat. Mater.* **17**, 63–71 (2018).
45. Ahn, J. & Na, S.-J. Three-dimensional thermal simulation of nanosecond laser ablation for semitransparent material. *Appl. Surf. Sci.* **283**, 115–127 (2013).
46. Johnson, P. B. & Christy, R. W. Optical constants of the noble metals. *Phys. Rev. B* **6**, 4370–4379 (1972).
47. Hirt, C. W. & Nichols, B. D. Volume of fluid (vof) method for the dynamics of free boundaries. *J. Comput. Phys.* **39**, 201–225 (1981).

ACKNOWLEDGEMENTS

This research is supported by A*STAR under its AME IRG Grant (Project No. A20E5c0091).

AUTHOR CONTRIBUTIONS

L.W. performed the multiphysics thermal-fluid flow simulation and analysis, and drafted the manuscripts. Y.Z. and H.Y.C. checked the simulation results and revised the manuscript. W.Y. conceived the project and led the study. All authors contributed to the discussion of the project and manuscript preparation.

COMPETING INTERESTS

The authors declare no competing interests.

ADDITIONAL INFORMATION

Supplementary information The online version contains supplementary material available at <https://doi.org/10.1038/s41524-022-00699-6>.

Correspondence and requests for materials should be addressed to Wentao Yan.

Reprints and permission information is available at <http://www.nature.com/reprints>

Publisher's note Springer Nature remains neutral with regard to jurisdictional claims in published maps and institutional affiliations.



Open Access This article is licensed under a Creative Commons Attribution 4.0 International License, which permits use, sharing, adaptation, distribution and reproduction in any medium or format, as long as you give appropriate credit to the original author(s) and the source, provide a link to the Creative Commons license, and indicate if changes were made. The images or other third party material in this article are included in the article's Creative Commons license, unless indicated otherwise in a credit line to the material. If material is not included in the article's Creative Commons license and your intended use is not permitted by statutory regulation or exceeds the permitted use, you will need to obtain permission directly from the copyright holder. To view a copy of this license, visit <http://creativecommons.org/licenses/by/4.0/>.

© The Author(s) 2022